Dynamic damage in carbon-fibre composites

DOI:
10.1098/rsta.2016.0018

Document Version
Accepted author manuscript

PHILOSOPHICAL TRANSACTIONS A

rsta.royalsocietypublishing.org

Research

Cite this article: Bourne NK, Parry S, Townsend D, Withers PJ, Soutis C, Frias C. 2016 Dynamic damage in carbon-fibre composites. *Phil. Trans. R. Soc. A* **374**: 20160018. http://dx.doi.org/10.1098/rsta.2016.0018

Accepted: 22 February 2016

One contribution of 22 to a Theo Murphy meeting issue 'Multiscale modelling of the structural integrity of composite materials'.

Subject Areas:
materials science, mechanics, wave motion

Keywords:
dynamic loading, damage, composite failure, Taylor's test

Author for correspondence:
N. K. Bourne
e-mail: neil.bourne@manchester.ac.uk

Dynamic damage in carbon-fibre composites

N. K. Bourne[1,2], S. Parry[2,3], D. Townsend[2], P. J. Withers[1], C. Soutis[1] and C. Frias[1]

[1]School of Materials, University of Manchester, Manchester M13 9PL, UK
[2]Centre for Matter under Extreme Conditions, School of Materials, Rutherford Appleton Laboratory, Didcot, Oxfordshire OX11 0FA, UK
[3]Defence Science and Technology Organisation, PO Box 1500, Edinburgh, South Australia 5111, Australia

NKB, 0000-0002-8883-1196; CS, 0000-0002-1402-9838

The Taylor test is used to determine damage evolution in carbon-fibre composites across a range of strain rates. The hierarchy of damage across the scales is key in determining the suite of operating mechanisms and high-speed diagnostics are used to determine states during dynamic loading. Experiments record the test response as a function of the orientation of the cylinder cut from the engineered multi-ply composite with high-speed photography and post-mortem target examination. The ensuing damage occurs during the shock compression phase but three other tensile loading modes operate during the test and these are explored. Experiment has shown that ply orientations respond to two components of release; longitudinal and radial as well as the hoop stresses generated in inelastic flow at the impact surface. The test is a discriminant not only of damage thresholds but of local failure modes and their kinetics.

This article is part of the themed issue 'Multiscale modelling of the structural integrity of composite materials'.

1. Introduction

Understanding damage progression and failure in composite materials is critical for reliable and cost-effective engineering design. Damage within composites can take a range of different modes according to load and architecture including cracking, breakage and

THE ROYAL SOCIETY PUBLISHING

buckling [1]. These macroscale responses result from microscale processes operating at mesoscale material interfaces and thus there is a suite of physical mechanisms that underlie the nucleation and progression of damage under mechanical load in these materials [2,3].

Here the scales accessed in the deformation of a carbon-fibre composite (CFC) are explored under dynamic loading. Polymer matrix composite panels are typically made up from a series of unidirectional plies, variously oriented so as to give a quasi-isotropic in-plane response. In contrast with conventional monolithic materials, the composite behaviour is dominated by the many interfaces between matrix and fibres and between the individual plies. Thus, delamination (interlaminar) strength is much lower in these materials (lack of fibres in the through-the-thickness direction), while microscale failure within the carbon fibres is governed by localization and fracture of the fibres at a much lower scale and at higher stresses. Thus, mesoscale mechanisms operating in the composite considered here include the nucleation of matrix fracture at defects which starts fibre/resin debonding, leading then to ply debonding (delamination) and subsequently fibre fracture, causing ultimate laminate failure [3].

A dynamic test probes different failure modes at different scales since the stress field is not steady until waves have equilibrated the state throughout the cylinder [4]. Of course, in reality the stress state is always fully three dimensional at scales below a representative volume element for the microstructure as the composite fibres and their geometrical plies sit within a polymer matrix with different mechanical properties. Further at the lower length scales, the material is highly anisotropic with local moduli varying by orders of magnitude in individual phases. Thus multiaxial loading in the Taylor geometry, and the composite nature of the microstructure at the mesoscale, results in a range of observed operating mechanisms occurring in compression but also in tensile failure on release [5].

Engineering numerical models require a constitutive law for the compressive response with an often separate damage model running in parallel. While models generally operate at the macroscale, this simple validation experiment has a suite of responses that occur at lower scales. Given the complexity of, and interplay between, the available suite of operating mechanisms such material systems pose a considerable challenge to reproduce effects observed experimentally in simulation.

In its original form, the Taylor test (figure 1) was designed as a simple laboratory experiment in which a cylinder of a test material impacts a rigid anvil and expands at a frictionless contact on its surface [6]. As seen above, a range of different mechanisms at different length scales operate and lead to a macroscopic response conditioned by both macroscale inertial constraints and mesoscale damage mechanics [6–8]. The modern adaptation of the Taylor test is a fully integrated experiment that records both the macroscopic behaviour but allows interrogation of a range of these mesoscale physical mechanisms. It has been extensively used in constitutive model validation for metals, but has not been employed widely for other classes of material [9–12]. There has been some recent use in polymers, but little in continuous fibre-reinforced composites to date [13–17]. In particular, after a loading phase that is first controlled by compression and viscoplastic flow, there is a second that follows and includes release and failure which may be by fibre tensile fracture, delamination or fibre microbuckling/kinking. This latter phase affords a means of studying three independent modes of failure in one geometry and shows distinct regions of deformation that are separated in position and in time and are accentuated in the composite cylinder observed here. The head of the rod, and only a central conical portion of it, experiences a shocked state. In this phase of loading, the global stress state is inhomogeneous. Within one diameter of the impact face, the loading front has exited this one-dimensional strain state and entered an axisymmetric loading phase dominated by a decaying elastic front travelling towards the rear of the cylinder. The loading modes and their different nature and effect are discussed elsewhere [4].

This work illustrates the differing responses in compression and shows markedly different failure characteristics of three rods cut from the same nominally two-dimensional composite architecture but in different orientations. In particular, it shows that the hierarchy of microstructural length scales is not necessarily the same in the compression phase as for damage

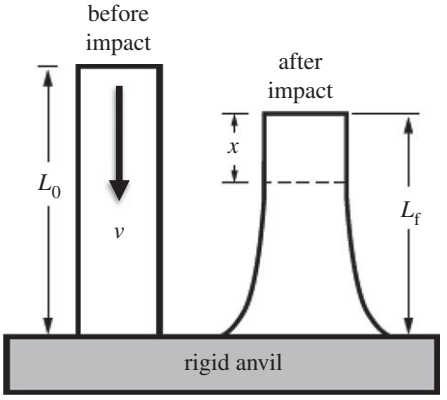

Figure 1. The Taylor impact test [6]. A right cylinder is projected onto a rigid anvil and inelastic deformation in the shocked zone at the impact face deforms it and instigates damage in various modes as waves equilibrate the stress state within the cylinder.

in tension and shear. Thus, further work is necessary to understand response and damage mechanics to properly represent constituent properties with numerical codes for design and evaluation of composite response. However, it clearly indicates the utility of such a simple test to understand and rank composite dynamic performance in engineering applications.

2. Material properties and impact experiments

The composite, multi-layered panel was constructed from autoclave-cured, pre-impregnated (pre-preg) sheets, made from unidirectional, intermediate modulus carbon fibres encased within a toughened epoxy (figure 2). These 0.125 mm pre-preg sheets were layered alternately in 0° and 90° orientations to a final panel thickness of approximately 25 mm. The composite panel had a density of $\rho_0 = 1.4\,\mathrm{g\,cm^{-3}}$. The different phases had the following nominal mechanical characteristics where the subscript C refers to the fibres and E to the bonding epoxy resin matrix: $\rho_C = 1.8\,\mathrm{g\,cm^{-3}}$, $\rho_E = 1.2\,\mathrm{g\,cm^{-3}}$, $K_C = 65.6\,\mathrm{GPa}$, $G_{1C} = 55.5\,\mathrm{GPa}$, $K_E = 5.4\,\mathrm{GPa}$ and $G_E = 2.5\,\mathrm{GPa}$, where K and G are the respective bulk and shear moduli.

Right cylinders were machined with the cylinder axis within the plane at 0°, 45° and with it oriented through-thickness (TT) to the panel as shown in figure 2. The cylinders had a diameter of 7.6 mm, a length of 22.5 mm (or 38.0 mm) and a mass of *ca* 1.6–2.7 g giving an approximate length to diameter ratio of 3 : 1 (or 5 : 1).

Taylor's tests were performed on these composite cylinders. They were fired from a single stage gas gun, onto a hardened steel anvil [18]. Molybdenum disulfide grease was used on the surface of the anvil prior to each impact to ensure that the coefficient of friction between anvil and cylinder was kept as close to zero as practicable. A digital high-speed camera, operating at approximately 120 000 frames $\mathrm{s^{-1}}$ (8 μs interframe time (IFT)) and with a 1 μs per frame exposure time (ET), was used to record the sequence of damage events. In all cases, a range of impacts with speeds in a range from below 100 to above 300 $\mathrm{m\,s^{-1}}$ were conducted in order to observe distinct failure modes within the composite.

In all of the tests, high-speed imaging was used to track quantitative macroscopic deformation. The camera simultaneously recorded frames as well as streak imaging down both an impact axis and in the plane of the impact on the anvil surface. The images are presented conventionally with the spatial axis running horizontally and the temporal running vertically. A typical framing sequence for impact of a CFC rod is shown in figure 3*a*. The motion of the rod and waves within the experiment were analysed using streak photography and the two streak axes are illustrated in figure 3*b*. Figure 3*c* shows in the central two images the *y*-streak direction showing

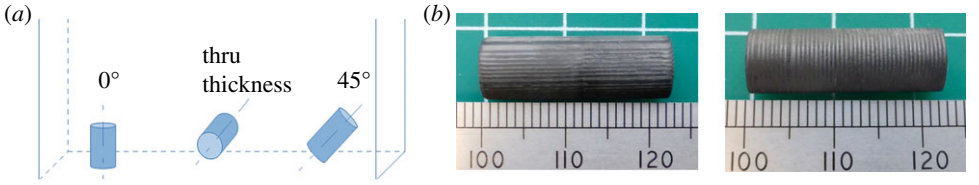

Figure 2. Carbon-fibre composite Taylor samples; (*a*) cylinder orientations with respect to the composite plate, (*b*) in-plane 0° and through-thickness (TT) samples before firing. (Online version in colour.)

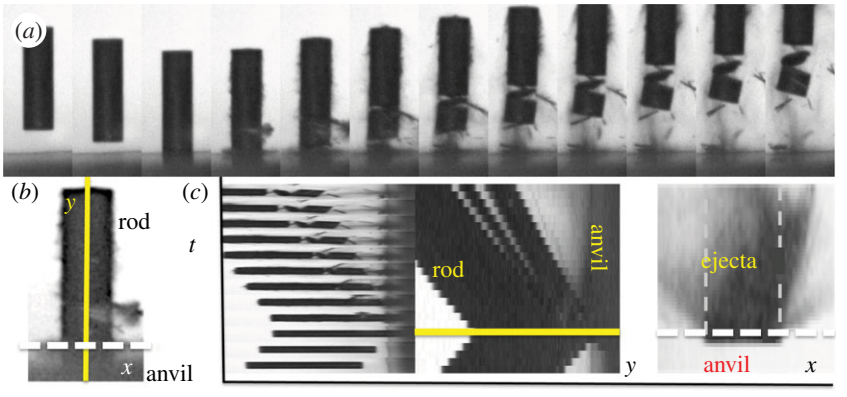

Figure 3. (*a*) Impact of a composite cylinder cut in the TT direction. Impact velocity 153 m s^{-1}. IFT in (*a*) is 8 µs and each frame of the sequence runs from left to right. (*b*) Definition of the streak axes; *x* in the plane of impact and *y* in the impact direction are superimposed on frame 4 of the sequence in (*a*). (*c*) *y*-(made up from a and the recorded image) and *x*-streak records illustrating rod impact onto the anvil (*y*-axis) and ejecta motion from the surface (*x*-axis). Here the sequence is rotated so that distance *y* runs horizontally and time *t* vertically (upwards). (Online version in colour.)

the correspondence between the shrinking and rotation of the framing sequence and the *y*-streak, and the *x*-streak to the far right.

The cylinders were fired from a single stage gas gun using helium or nitrogen driver gases. Impact was onto a hardened steel anvil and targets were aligned for normal impact to within 10 mrad to control obliquity [18]. Molybdenum disulfide (MoS_2) grease was applied to the surface of the anvil to prevent friction at the impact face. A digital high-speed camera (Vision Research Phantom V12), operating at 120 000 frames s^{-1} (8 µs; FT) and with a 1 µs frame ET, was used to record the events.

3. High-speed imaging of impact

In the following sections, the responses of Taylor's cylinders impacting the anvil in the geometry of figure 1 are shown for a range of impact velocities and for the three sample orientations through the composite panel described above. Selected sequences typical of the observed behaviours for each of the three sample types (0°, 45° and TT). As one might expect, given the 0°/90° ply arrangement, samples cut at in-plane 90° ply orientation behaved in an identical manner to the 0° samples and thus these results are not reproduced here. In all cases, the high-speed photographic sequences are presented as a series of frames moving forward in time left to right (and top to bottom if applicable). The *x*- and *y*-axes are indicated on each figure and corresponding streaks are to the centre and right. The labels (*a*), (*b*), etc. refer to different experiments in each case.

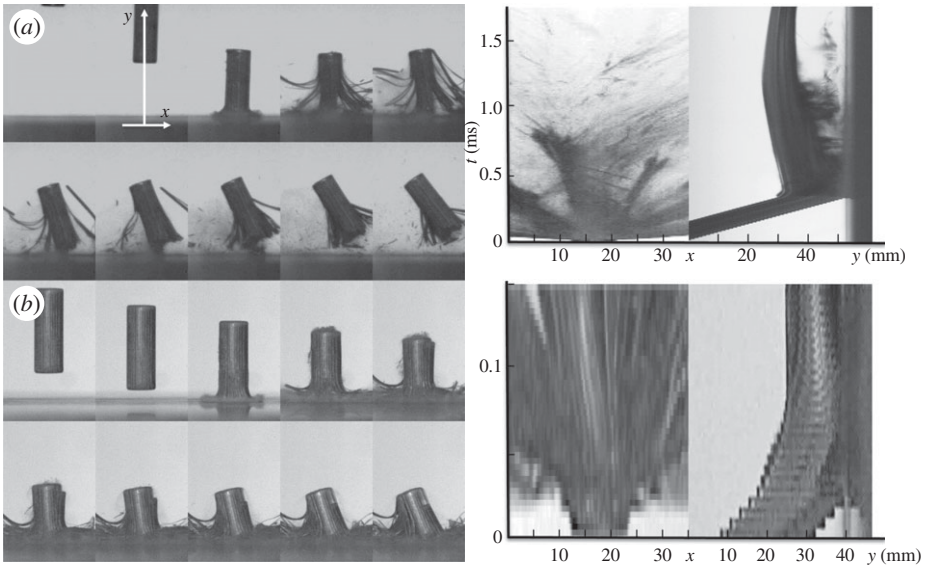

Figure 4. Impact response of 0° composite Taylor cylinders. Impact at (*a*) 148 m s^{-1} and IFT = 125 µs and (*b*) at 268 m s^{-1} and IFT = 17 µs (left) successive time frame images and (right) streak images for *x*- and *y*-directions shown to the right with common time axis, *t*, for each impact.

(a) Impact of in-plane (0°) samples

Figure 4 shows two impacts at 148 and 268 m s^{-1} conducted on 0° samples. The lower speed sequence (in figure 4*a*) is above the threshold at which delamination first begins. It is observed to first occur at the edges of the impact face when velocities exceed around 50 m s^{-1}. This corresponds to a stress induced at impact of *ca* 200 MPa. The point at which deformation starts (frame 3) shows symmetrical expansion of the impact footprint and delamination can be seen in the first frames. The first indication of fibre-end fracture against the surface of the anvil can be seen in frame 4. The failure of these fibres, particularly in the outermost region, creates a fragment field with sub-millimetre fibre remnants visible at the anvil surface. These expand outward in a cloud from the impact surface and much of the impact energy is taken in matrix fracture and in delamination by interlaminar shear. In this particular case, the elastic deformation of the left-most fibres bend and then release the outer ones springing this region back off the surface and rotating the remaining damaged cylinder in the surface zone. This asymmetry means that delamination does not continue to the rear surface on the LHS while the free surface that opens on the RHS allows delamination to (in this case) just reach the rear surface for the outermost plies. A white dot superposed on the rear of the cylinder and visible through the impact indicates that in this launch there is minimal barrel rotation so that this asymmetry results from purely material defects within the composite leading to inhomogeneous failure within the test.

In frame two of the sequence, two axes (*x* and *y*) are superposed onto one image of the cylinder. These represent the two directions in the impact for which streak images have been recorded and shown to the right of the framing sequence. The central *x*–*t* image shows the intrusion of the rod onto the impact surface and its diameter spreading for the contact time with fragments flowing outward from the impact zone. There are two symmetrical dark regions exiting the surface. The shallow angle lines are due to surface fibre fracture and expulsion in a cloud with the lubricating grease. The higher angle represents the expansion of the external edges of the cylinder after debonding of the fibres and plies to accommodate the lateral strain. The *y*–*t* (furthest right) shows the rod entering the field of view, impact on the surface and return of the wave from the impact face. It shows that the rear of the rod has initially rebounded but then rotated

within a diameter of the surface for the remaining time. For a fully three-dimensional loading geometry this one-dimensional projection cannot interrogate all phases of loading on the anvil. However, in combination with framing information and during the controlled phases of loading in this experiment it allows a valuable quantitative picture of interface and wave behaviour to be obtained for these materials.

Figure 4*b* shows the impact of a cylinder at 268 m s^{-1} from the same 0° cut. Although the delamination and interlaminar shear response is qualitatively similar to that seen for the lower speed sequence, the macroscopic behaviour is more homogeneous. This stress level represents a further threshold in micromechanical behaviour for the material under load. There is now more uniform surface damage in the rod with buckling and failure of all the fibres within a diameter of the impact face. Further interlaminar failure propagates to the rear of the cylinder on all planes at this velocity and greater (although this rod is $L/D = 3$ and thus shorter than that in figure 4*a*). However, at this speed there is also fibre fracture on the surface and also delamination within the central core where material is inertially confined. Again delamination is not uniform but at the higher impact stresses this effect is less pronounced and the response is more homogeneous with strain accommodated by buckling and fracture in the fibres. This deformation is concentrated in the region one diameter from the anvil surface and couples with that deposited in delamination of the fibre plies at sites away from the surface impact zone.

The central x–t streak shows the intrusion of the rod onto the impact surface but now deformation is localized and uniform across the surface zone. Some evidence of the flow of outer parts of the core at greater diameters is evident at later times. The y–t streak (furthest right) shows the rod entering, impact on the surface, an inelastic flow region in deformation and finally rest of the remnant cylinder onto the surface. It illustrates that this speed represents a threshold beyond which a pseudo-hydrodynamic response for this composite structure may be used to describe response. Of course, there is some time taken for this process to begin and this corresponds to the transit of delamination down the rod under this stress state (around 1 GPa at this speed). A macroscopic continuum mechanics-based constitutive model has been shown to have success in representing the macroscopic damaged state for this material and is presented in a companion paper [19].

(b) Impact of in-plane (45°) sample

Figure 5 shows the impact of a 45° laminate at 213 m s^{-1}. The response is qualitatively similar to that at other speeds for this type of sample over the velocity range considered. The shock stress level is *ca* 0.8 GPa at the impact face in this case. The IFT for this sequence is 42 µs per frame. The impact causes immediate delamination of the incoming composite panel (see frame 4 onwards). The principal operating deformation mechanism is shear-induced microfracture and the 45° lay-up leads to easy delamination and flow for the composite under impact since it lies down the plane of principal shear. The region no more than one diameter from the impact (subject to the highest stresses) fails and flows easily over the first frames. Very quickly there is failure down the confined core fibre region (which required much higher velocities in the case of the 0° case) and fracture extends more easily back to the rear surface opening two hinged struts (see frame 5 onwards) that rapidly collapse the bulk of the material onto the surface accommodating the impact energy in flow. In contrast with the impact of the other samples there is little debris ejected around the site and fibres are kept largely intact within the opening fragments. This shows the ease of delamination (scissoring response) in this geometry relative to other modes of failure with less energy expended in fibre crushing and fracture.

The x-streak image shows easy break-up and surface flow relative to the more inhomogeneous and extended failure for the 0° case despite the impact velocity in that case being 25% greater (and the input kinetic energy thus being *ca* 60% more). The y-streak shows graphically the macroscopic response of the cylinder in this geometry as it impacts and then collapses and flows across the anvil. It should be compared with figure 4*b*, where the y–t streak shows the shortened cylinder essentially stationary at the surface despite the higher impact velocity.

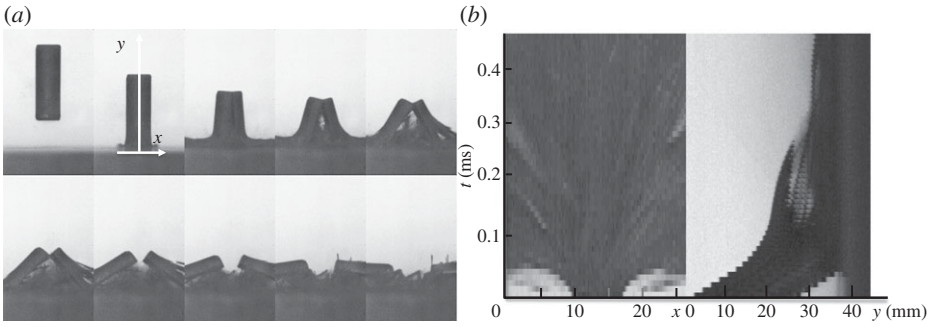

Figure 5. (*a*) Time-lapse sequence showing the impact response of a 45° composite cylinder. The IFT for this sequence is 42 µs per frame and the impact velocity 213 m s^{-1}, (*b*) streaks for the *x*- and *y*-axes (cf. figure 4*b*).

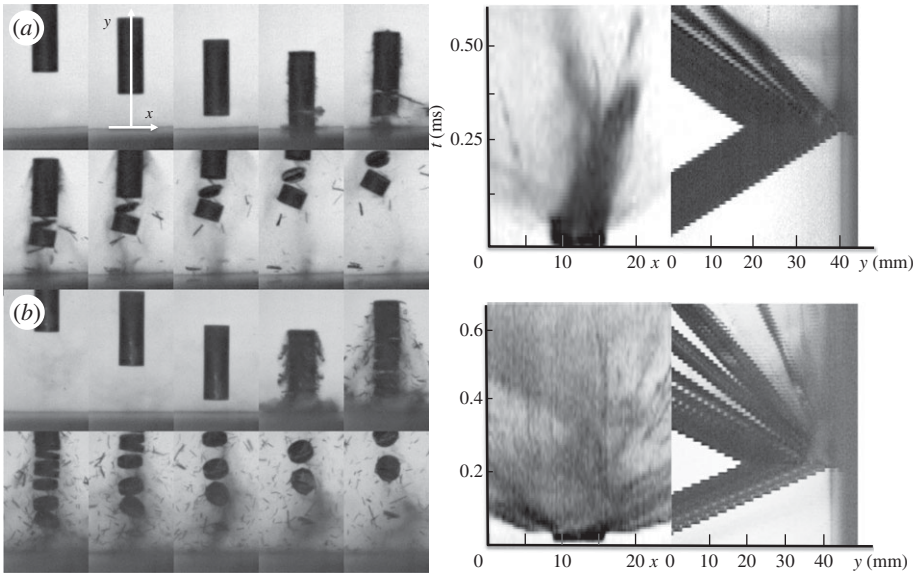

Figure 6. (left) Impacts onto through-thickness (TT) composite cylinders. (*a*) IFT 42 µs impact velocity 153 m s^{-1} and (*b*) IFT 42 µs impact velocity 246 m s^{-1} (right) streak images for the *x*- and *y*-axes.

(c) Impact of through-thickness samples

Figure 6 shows the response of cylinders cut in the TT direction to the impact axis. At the lower speed of 153 m s^{-1} it has around the same kinetic energy as that of figure 4*a*. The shock stress level is *ca* 0.6 GPa at the impact face in this case. The response is however very different to those for samples cut in either of the other directions shown. Frame 7 shows a puff of dust as the epoxy laminate fails and dust and a plane of plies are expelled outwards and to the right. This first failure occurs at slightly less than one diameter from the impact face. It corresponds to the end of the shocked zone in the composite and the point at the end of the region in which lateral releases combine down the central axis. Later frames show that this corresponds to the failure of the surface impact plug and also a single adjacent ply at this position that is seen detaching (and rotating) through subsequent frames. Of course, a longitudinal release fan propagates from the free rod surfaces and this will disperse tensile loading across several fibre planes. There is a sparse population of damaged fibres seen expelled in crushing at the impact face and also in the vicinity of the delamination plane in this geometry. These amount to a few isolated fibres that

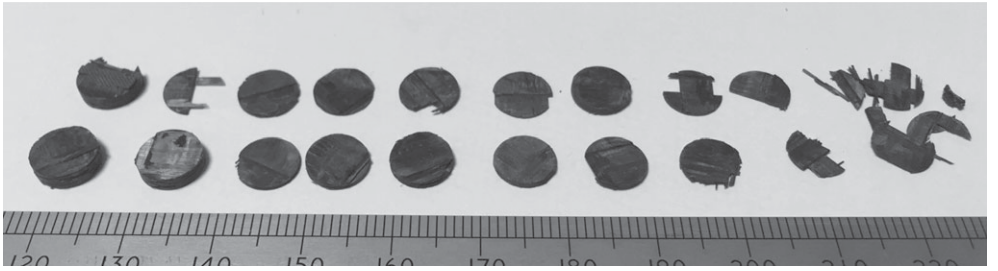

Figure 7. Recovered discs from the impact of a TT cylinder at a velocity of 246 m s^{-1} (see sequence figure 6*b*).

have little momentum and whose ejection absorbs negligible energy. This sequence represents the threshold at which the cylinder is first failed in this mode. It is interesting that this is at the same impact stress level at which complete delamination occurred for the 0° sample (figure 4*a* and indeed similar tensile stress levels will be acting in the two cases on fibre plies although of course acting in different directions.

The *x*-streak at the anvil face shows graphically that the impact and rebound are largely elastic. There is little expansion of the cylinder on the surface and the grey areas correspond to ejected grease not failed material in this image. The *y*-axis streak, on the other hand, indicates the almost rigid body nature of the impact and graphically illustrates the response of the composite. The rear two segments of the cylinder rebound elastically as can be seen (since the slope of the rear interfaces show the rebound to be the negative of the incoming cylinder), while the expelled rotating disc and the plug travel more slowly from the surface. The rear of the cylinder shows a more subtle change in slope on the return of the compression wave from the impact face and a subsequent slight deceleration of the cylinder on the rebound. This impact speed represents the onset of interlaminar fracture in the cylinder and occurs behind the zone of compression that exists on the surface.

Figure 6*b* shows the response when a much higher impact pressure is induced and the composite is unzipped into a stack of failed discs by wave interactions in the cylinder. Again the IFT is 42 µs but the impact velocity is in this case 246 m s^{-1} which induces an impact stress of *ca* 0.9 GPa. The shocked surface zone (and now the rest of the incoming column) has bonded regions between the plies rapidly failed by the returning compression wave that then reflect as an elastic tensile pulse. As seen earlier this does not fail the original (as-received) material but now merely unzips a stack of adjacent stacked platelets with failed plies between each. The greatest velocity is imparted to that zone where the release reaches first and the ejected disc traps most of the original momentum within it bouncing back at almost the incoming rod speed. Further discs receive gradually less returning longitudinal release impulse as the wave decays down the stack expending energy failing the zone damaged in compression.

The *x*-streak for the impact shows little lateral expansion on the anvil face (as was the case for the lower speed impact) yet a cloud of failed fibres entrained in grease from the impact face can be seen emanating from the impact zone. The *y*-streak shows graphically the expanding stack of discs under the returning release front from the rear surface. The top of the stack seen here has almost the same speed as the incoming cylinder and the slowing velocity of each segment reflects energy expended in failing planes down the cylinder as it fragments layer by layer. The larger fragments are at the rear of the rod where the compression wave has induced less damage and the greater failure and fragmentation is in the surface zone as expected. There is little or no rear surface ejecta but there are sprays seen at the failing composite planes expelled laterally during impact. Nevertheless, there is little inelasticity seen in any of the rapid interlaminar failures. Viewed as a macroscopic illustration of impact behaviour, the sequence shows the transition from solid to hydrodynamic deformation as the composite deforms.

Figure 7 shows the recovered discs from the impact of the sample shown in figure 6*b*. An array of failed surfaces is evident with recovered fragments from the impact region at the right-hand

side and large segments to the left from the distal end. Light reflecting back off the fractured surfaces illustrates the brittle nature of the response and the planarity of these surfaces shows the geometrical alignment of the release front direction and the vector normal to the fibre plies lay-up plane. It is clear that local microfracture is the operating inelastic deformation mechanism in this case.

4. Discussion

The global response of the TT cylinder shows important features of composite response. As an aside it is worth considering global momentum transfer and its effect upon a cylinder during loading and unloading in the elastic impact of an isotropic material. The unloaded target cylinder can be considered as a stack of elemental disc-shaped elements in uniform motion, a face of which is stopped by the rigid anvil on impact. Thereafter, these elements are sequentially decelerated by a compression front that travels back up the cylinder taking the velocity of each element to rest. On reaching the rear of the cylinder the wave reflects and subsequent elements are now accelerated to precisely the speed of the incoming cylinder in an opposite direction. In an inelastic Taylor's impact some fraction of the kinetic energy is dissipated in damage processes within the cylinder and the rebound speed is lower than that at impact. Lateral waves release the free surfaces in a front that travels into the centre and upwards through the cylinder interacting with surfaces again one rod diameter from the impact face. These also travel upwards through the cylinder and reach the rear face at the end of the compression phase interacting with lateral surfaces as they do so. In the case of the material considered here, the lay-up of the composite results in a material with orthotropic properties in which wave speeds in the lateral (in the $0^\circ/90^\circ$ plane) and longitudinal (TT) directions are in ratio *ca* 1 : 2.3. Thus, the first interactions of lateral waves with surfaces occur not at one diameter (D) (and subsequent integer fractions) back from the impact surface but at *ca* $0.3D$ and multiples thereof.

Secondly, a composite material with an array of phases and an anisotropic yield surface is subjected to a range of compression and release states under Taylor's impact with each experiencing a unique release strain state during the process. The flow is globally two dimensional but locally three dimensional at the mesoscale. In this test, and in the response of composites in the general case, failure occurs first at the mesoscale boundaries between phases so that the microscale inelastic behaviour of individual constituents is rarely significant to its engineering response. Thus, the key physical mechanisms are operating on a length scale beneath the observed observations made at the macroscale with high-speed imaging. Nevertheless, their effects on response and the kinetics of their operation are measureable at the laboratory scale. The principal failure mechanisms observed are nucleation and local matrix fracture that itself subsequently propagates and results in fibre/matrix debonding. The microscale processes are those of nucleation and propagation of local failure between fibre planes, which lead to delamination and then fibre compression and buckling followed by fracture and fragmentation. Each of these damage processes reduces the integrated strength of a volume element at the scale above the one within which failure occurs.

In the first moments, the impact face is shocked and a pressure of *ca* 0.5 GPa at the lower velocity ($150\,\mathrm{m\,s^{-1}}$) and 1 GPa at the higher ($250\,\mathrm{m\,s^{-1}}$) is applied to the composite. In the compression phase, the fibre/binder layer sees intense shear and boundaries are frequently failed during the passage of the shock [8]. The wave decays as lateral release propagates into the damage zone from the periphery expanding the volume radially and opening microfractures. This allows free fibres to expand outward or to buckle and break on the hard anvil surface according to their position and thus their confinement. The wave interactions result in a release fan which meets down the cylinder axis and here loads the surface zone in tension down the impact axis. In metals (particularly those in which dislocation flow is easy), this results in ductile void formation on the axis. In the composite, it nucleates failure at mesoscale flaws. Finally, reflection of the compression wave arrests and then accelerates material back in the impact direction and again if

this wave can overcome further damaged interfaces, components of the composite fail down the cylinder back to the impact face. Thus, there is a single compression phase in which damage may occur and three possible tensile failure modes within the brief duration of the impact. Each state has an operational time over which different components of the microstructure and different deformation mechanisms operate at different scales.

Figure 6*b* and the recovered fragments of figure 7 illustrate each of these failure modes. The cylinder is failed by a compression pulse travelling from the impact region that attenuates as it proceeds down the rod. Thus, the degree of damage decreases as it progresses as can be seen in the fragments recovered. Frame 5 of figure 6*a* and frames 4 and 5 of figure 6*b* show the arrival of lateral waves failing planes within the cylinder and expelling a puff of failed debris at these positions. This includes intact plies of material in some cases and failed fibres in others. The reader will note that these remaining discrete pucks of material have thickness around 30% of the diameter of the cylinder and this results from lateral wave propagation speeds within the orthotropic composite discussed above. The rear of the cylinder releases first on reflection of the front and does so at the impact speed. Damaged blocks of composite follow it at a similar speed. As the release reaches the impact zone, more and more energy is dissipated in failing the damage zones induced there. The final segment to leave the surface is a thin sheet detached at the impact surface itself and travelling at around 20% of the impact speed. However other blocks are travelling at *ca* 30% and greater and so the fragments separate. Note that the *y*-streak for the $150\,\mathrm{m\,s^{-1}}$ impact is similar to that at $250\,\mathrm{m\,s^{-1}}$. This reflects the greater level of damage at this position at the first release point where most of the inelastic work is done. Of course, as impact velocity is increased this surface zone will experience increasing local fracture, but the release interaction will act as a geometrical constraint that will localize damage in this region.

5. Conclusion

Each of these modes of loading is illustrated for the orthotropic composite placing the weak interlaminar planes in different orientations to loading leading to differing failure modes. Since different damage mechanisms are activated in each case, the strengths of the interfaces between each composite components at different strain rates is probed.

The Taylor test is used here is a useful descriptor for failure and is a rigorous test of constitutive models for composite response in compression, tension and shear [6]. Careful design of the velocities and geometries of the loading allows composite damage to be localized by design by using release interactions to probe weak interfaces within the microstructure. The loading sweeps the impacted cylinder with a compressive wave that localizes deformation and nucleates damage sites in the inhomogeneous stress state induced. These defects, nucleated under compression at the micro-, meso- and structural scales, have a different hierarchy to those for damage in this case. Indeed the transit from nucleation of defects via propagating micromechanisms to the failure of the structure span different times and scales within the loading. The micromechanisms induced include matrix cracking which couples to matrix debonding, delamination and fibre cracking leading to structural breakage at the macroscale.

This work has shown that cylinders cut down varying directions in an orthotropic material show a suite of responses to simple applied loading at a rigid anvil. The step in compressive stress applied to the cylinder on impact sweeps down it and decelerates the target. The later release and rebound reveal the damage incurred in the compressive phase in deformation at the macroscale. Experiment has shown that ply orientations respond to two components of release; longitudinal and radial as well as the hoop stresses generated in inelastic flow at the impact surface. The TT direction fails entirely down the length into platelets at damage planes induced down the impact axis during compressive loading. In the in-plane geometry, however, damage initiates after lateral release in the first diameter and fractures the cylinder by interlaminar debonding.

The test discriminates between different failure mechanisms in a loaded composite across all modes of loading and as such can be used to assess new structural composite designs as well as in validation of numerical simulations using new constitutive descriptions. Coupled with dynamic and tomographic identification of failure, the technique has shown great promise as a quantitative dynamic failure test for composites to determine operating mechanisms, screen new composite lay-ups and observe macroscopic high-rate response as well as serving its principal use in recent times in validating the most modern constitutive descriptions [19]. In summary, this test is a simple and reproducible way of investigating physical operating mechanisms for a composite under dynamic load and may be used as a screening test for composites used in such environments.

Competing interests. We declare we have no competing interests.

Funding. We received no funding for this study.

Acknowledgements. We thank the university technical support in particular Ryan Delve for his enthusiasm and skill in maintaining the facilities.

References

1. Hughes JDH. 1991 The carbon fibre/epoxy interface—a review. *Compos. Sci. Technol.* **41**, 13–45. (doi:10.1016/0266-3538(91)90050-Y)
2. Fleck NA, Jelf PM, Curtis PT. 1995 Compressive failure of laminated and woven composites. *J. Compos. Technol. Res.* **17**, 212–220. (doi:10.1520/CTR10485J)
3. Jelf P, Fleck N. 1992 Compression failure mechanisms in unidirectional composites. *J. Compos. Mater.* **26**, 2706–2726. (doi:10.1177/002199839202601804)
4. Bourne NK. 2013 *Materials in mechanical extremes: fundamentals and applications*. Cambridge, UK: Cambridge University Press.
5. Taylor GI. 1946 The testing of materials at high rates of loading. *J. Inst. Civil Eng.* **26**, 486–519. (doi:10.1680/ijoti.1946.13699)
6. Taylor GI. 1948 The use of flat ended projectiles for determining yield stress. I. Theoretical considerations. *Proc. R. Soc. Lond. A.* **194**, 289–299. (doi:10.1098/rspa.1948.0081)
7. Whiffin AC. 1948 The use of flat ended projectiles for determining yield stress. II. Tests on various metallic materials. *Proc. R. Soc. Lond. A.* **194**, 300–322. (doi:10.1098/rspa.1948.0082)
8. Woodward RL, Burman NM, Baxter BJ. 1994 An experimental and analytical study of the Taylor impact test. *Int. J. Impact Eng.* **15**, 407–416. (doi:10.1016/0734-743X(94)80025-5)
9. Foster Jr JC, Maudlin PJ, Jones SE. 1996 On the Taylor test: a continuum analysis of plastic wave propagation. In *Shock Compression of Condensed Matter 1995, Proc. Conf. of the American Physical Society Topical Group on Shock Compression of Condensed Matter, Seattle, WA, 13–18 August* (eds SC Schmidt, WC Tao), pp. 291–294. Woodbury, NY: American Institute of Physics.
10. Jones SE, Maudlin PJ, Foster Jr JC. 1997 An engineering analysis of plastic wave propagation in the Taylor test. *Int. J. Impact Eng.* **19**, 95–106. (doi:10.1016/S0734-743X(96)00020-6)
11. Maudlin PJ, Foster Jr JC, Jones SE. 1997 A continuum mechanics code analysis of steady plastic wave propagation in the Taylor test. *Int. J. Impact Eng.* **19**, 231–256. (doi:10.1016/S0734-743X(96)00021-8)
12. Maudlin PJ, Bingert JF, House JW, Chen SR. 1999 On the modeling of the Taylor cylinder impact test for orthotropic textured materials: experiments and simulations. *Int. J. Plast.* **15**, 139–166. (doi:10.1016/S0749-6419(98)00058-8)
13. Rae PJ, Brown EN. 2006 The Taylor impact and large strain response of PEEK. In *Shock Compression of Condensed Matter 2005, Proc. Conf. of the American Physical Society Topical Group on Shock Compression of Condensed Matter, Baltimore, MD, 31 July–5 August* (eds MD Furnish *et al.*), pp. 829–832. Melville, NY: American Institute of Physics.
14. Millett JCF, Bourne NK, Stevens GS. 2006 Taylor impact of PEEK. *Int. J. Impact Eng.* **32**, 1086–1094. (doi:10.1016/j.ijimpeng.2004.09.008)
15. Rae PJ, Gray III GT, Dattelbaum DM, Bourne NK. 2004 The Taylor impact response of PTFE (Teflon). In *Shock Compression of Condensed Matter 2003, Proc. Conf. of the American Physical Society Topical Group on Shock Compression of Condensed Matter, Portland, OR, 20–25 July* (eds MD Furnish, YM Gupta, JW Forbes), pp. 671–674. Melville, NY: American Institute of Physics.

16. Resnyansky AD, Bourne NK, Brown EN, Millett JCF, Rae PJ, McDonald SA, Withers PJ. 2015 Phase transition modeling of polytetrafluoroethylene during Taylor impact. *J. Appl. Phys.* **116**, 223502. (doi:10.1063/1.4903817)
17. Bourne NK, Brown EN, Millett JCF, Gray III GT. 2008 Shock, release and Taylor impact of the semicrystalline thermoplastic PTFE. *J. Appl. Phys.* **103**, 074902. (doi:10.1063/1.2891249)
18. Bourne NK. 2003 A 50 mm bore gas gun for dynamic loading of materials and structures. *Meas. Sci. Technol.* **14**, 273–278. (doi:10.1088/0957-0233/14/3/304)
19. Parry S, Resnyansky A, McDonald SA, Townsend D, Bourne NK, James BJ, Withers PJ. 2015 Impact and debonding of an armour composite. In *Shock Compression of Condensed Matter 2015, Proc. Conf. of the American Physical Society Topical Group on Shock Compression of Condensed Matter, Tampa, FL, 14–19 June* (eds R Chau, TC Germann, TD Sewell). Melville, NY: American Institute of Physics.